

Research Paper

Cross-scale refined analysis and reinforcement design for the rigid-flexible mixed region in hybrid dams

Musen Han^{a,b}, Kai Chen^{a,b,*}, Yelin Feng^c, Degao Zou^{a,b}, Qingfu Huang^c

^a The State Key Laboratory of Coastal and Offshore Engineering, Dalian University of Technology, Dalian, Liaoning 116024, China

^b School of Infrastructure Engineering, Dalian University of Technology, Dalian, Liaoning 116024, China

^c Kunming Engineering Corporation Limited, Kunming, Yunnan 650000, China

ARTICLE INFO

Keywords:

Hybrid dams
Scaled boundary finite element method
Cross-scale refined
Seismic response

ABSTRACT

To energizing implementation of “Carbon Peaking and Carbon Neutrality” strategy, a batch of pumped storage power stations represented by asphalt concrete panel dams have been planned in China. The safety assessment of the anti-seepage system is crucial to engineering construction. In this paper, a cross-scale approach and SBFEM are employed to investigate the deformation characteristics of a typical dam under various conditions, combining the generalized plastic model. The location of the weak area in the anti-seepage system is identified. Subsequently, a fresh step-type design is proposed based on simulations, aiming to enhance the stability performance of anti-seepage joint. The mechanism and influence of the step-type scheme are discussed from different perspectives through simulations. The research indicates that the asphalt panel slides along the underlying lapped concrete platform due to the uneven settlement between rockfill and concrete. Resulting in significant horizontal tensile strain at the top of the asphalt panel. The step-type design provides a positive reinforcement effect, significantly reducing slipping displacements along the interface and the tensile strain of the asphalt panel by hindering the slip path of the rockfill. An optimal range for the step-type design is recommended to be between 0.375 m and 0.45 m below the junction point. Additionally, a height of 0.45 m is suggested for the single-step form, while a height of 0.075 m is recommended for each step in the multiple-step form. For multiple steps, performance improves as the spacing between the steps increases. The adaptability of the panel to deformation is enhanced through the presented method, enhancing the safety margin of the anti-seepage system and offering guidance for similar projects.

1. Introduction

In recent years, renewable energy sources such as wind and solar power have been developed extensively by most countries to address energy crises and environmental pollution issues (International Renewable Energy Agency, 2020). However, the emergence of insufficient renewable energy consumption capacity has been observed in actual power system operation. The intermittency and fluctuation of renewable energy output result in low utilization efficiency (Pan et al., 2020; Javed et al., 2020). Among various energy storage technologies, pumped storage is the most mature and widely used. Pumped storage can effectively enhance the power system's ability to absorb new energy. Since the 1960 s, pumped storage power stations have been constructed extensively worldwide. By the end of 2022, the global installed capacity of pumped storage power stations reached 188.1GW. It is expected that

the global installed capacity of pumped storage power stations will increase by more than 50 % from the current level in 2023 (Development Situation and Outlook of Pumped Storage Power Stations., 2023).

As the core component of a pumped storage power station, the reservoir dam serves the functions of regulating water levels and storing water energy. Its safety is critical to the safe operation of the pumped storage power station. Reservoir safety can be compromised by factors such as reservoir leakage, dam slope sliding, and seismic damage. One of the most common issues in reservoir is leakage, which can impair the reservoir's storage function and, in severe cases, lead to dam failure. Therefore, the integrity of the anti-seepage system is essential to engineering safety. Hybrid dams, which are the primary type used for pumped storage power station reservoirs, are composed of concrete and panel dams. Uneven deformation in the rigid-flexible mixed areas of hybrid dams can cause slip and damage to the anti-seepage panel at the

* Corresponding author.

E-mail address: chenkai@dlut.edu.cn (K. Chen).

<https://doi.org/10.1016/j.compgeo.2024.106727>

Received 10 July 2024; Received in revised form 21 August 2024; Accepted 3 September 2024

Available online 7 September 2024

0266-352X/© 2024 Elsevier Ltd. All rights are reserved, including those for text and data mining, AI training, and similar technologies.

joints, affecting the dam's safe operation. For instance, the upper reservoirs of the Ludington Pumped Storage Power Station in the United States and the Waldeck-II Pumped Storage Power Station in Germany have experienced leakage around the inlet structures. Additionally, the leakage of the entire asphalt concrete panel occurred at the joint (Billington, 1998). The asphalt concrete panels of China's Niutoushan and Car Dam experienced excessive tension during the dam settlement process, resulting in cracks at the panel joints (Hao, xxxx). Ensuring the safety of seepage control in hybrid dams relies heavily on the seepage control panel. Researching joint optimization and reinforcement design is crucial for improving the safety margin of anti-seepage systems.

Dam engineering is characterized by large-scale structure and complex form. It's generally tens to hundreds of meters in height and exceeding one kilometer in length and width. The dam includes small-scale components such as anti-seepage panels, which have a minimum thickness of about 0.4 m. The scale of the structure varies greatly (Chen et al., 2018). Traditional numerical analysis of engineering structures oversimplifies models and materials, making it difficult to evaluate the performance of key structures in dams. To accurately identify significant structural weaknesses and reveal damage patterns and mechanisms, it is necessary to adopt refined cross-scale analysis methods. This is in line with the current trend in computational technology (Mao and Sun, 1991; Lee et al., 2003; Martin and Deschappelles, 2014; Zhang et al., 2017). Currently, the commonly used methods for cross-scale analysis include the following forms: 1) FEM-DEM coupling method, 2) Multi-point constraint method, 3) Consistent multi-scale method, etc. The FEM-DEM coupling method is mainly used to calculate structures with relatively small models, such as exploring the mechanical behavior of granular media (Guo and Zhao, 2014; Guo and Zhao, 2016) and the failure process of soil (Tu et al., 2017). The multipoint constraint method has yielded extensive research findings, but it is currently mostly applied to the calculation of small components and local structures, such as the dynamic characteristics of machine tools, sliders, columns, spindle shells, and other combined components (Brecher et al., 2016); as well as the mechanical properties of fiber-reinforced composite materials (Vorobiov et al., 2017). The development of consistent multiscale method has enabled fine analysis to practical engineering, such as describing the mechanical behavior of materials with complex microstructures (Liu et al., 2016) and studying local damage analysis of bridge structures (Chen et al., 2012; Li et al., 2010). However, discretizing the entire structure into solid units may result in low computational efficiency, as rods and similar elements aren't commonly found in geotechnical engineering structures. Consequently, there are few reports on fine analysis in geotechnical engineering. The methods described above have successfully achieved cross-scale analysis of complex structures and materials, yielding positive results. However, the above methods haven't been widely applied in the analysis of large-scale geotechnical engineering structures due to differences in engineering structures.

The scaled boundary finite element method (SBFEM) was proposed by Wolf and Song (Wolf and Song, 2000; Wolf and Song, 2001). It combines the advantages of the boundary element method and the finite element method. SBFEM can be used to calculate polygon elements that are difficult to solve using traditional methods. It offers several advantages, including semi-analytical high accuracy, dimensional reduction, and flexible grid. In recent years, SBFEM has been widely applied in analyzing dam-reservoir hydrodynamic interactions (Xu et al., 2018; Xu et al., 2016; Xu et al., 2017), electromagnetic problems (Liu et al., 2016; Liu and Lin, 2012); crack propagation problems (Goswami and Becker, 2012; Ooi et al., 2013; Ooi et al., 2016; Saputra et al., 2015), complex element analysis methods (Zou et al., 2017), porous media expansion (Zou et al., 2018), layered soil and soil-structure interactions (Lu et al., 2015; Birk and Behnke, 2012), wave interaction, and propagation simulations (Liu et al., 2012; Gravenkamp et al., 2017; Chen et al., 2014). However, radial analysis has limitations in the elastic-plastic field due to its inability to consider nonlinearity within the element. Ooi et al.

(Ooi et al., 2014) developed the polygonal scaled boundary finite element method using a nonlinear algorithm based on the least squares fitting of Gaussian integrals in the domain. This method addresses the limitations of SBFEM, which is restricted to analyzing elastic problems and has difficulty solving material nonlinearity. Chen et al. (Chen et al., 2017; Chen et al., 2018; Chen et al., 2019) constructed polygon and polyhedral shape functions based on elastic solutions of boundary lines, boundary surface Gaussian integrals and constant stiffness matrices. The elastic-plastic matrix and integral stress were calculated using Gaussian points within the domain. These studies developed the SBFEM polygon and polyhedral nonlinear analysis method, and pioneered its application in large-scale geotechnical engineering cross-scale fine analysis. For example, dynamic analysis of concrete face rockfill dam with complex spatial geometries and spanning huge scales (Chen et al., 2018), seismic cracking evolution for anti-seepage face slabs in concrete faced rockfill dams (Qu et al., 2020), refined analysis on stress state of cutoff wall of high asphaltic core dam on super-deep overburden (Zou et al., 2023) and so on. The application of SBFEM facilitates enhanced computational efficiency while maintaining the precision of crucial structural calculations. SBFEM holds significant promise for the analysis of large-scale geotechnical engineering structures.

In this paper, we investigated the deformation characteristics of typical dam that adopted the cross-scale approach and SBFEM proposed by the authors (Chen et al., 2017; Chen et al., 2018; Chen et al., 2019), combining the generalized plastic model. And the weak area in the anti-seepage system has been identified. Based on simulations and analyses, an innovative step-type design has been proposed, aiming to enhance the stability performance of anti-seepage joint. The mechanisms of the step-type, as well as the effects of step height and reinforcement depth, are discussed from various perspectives through simulations.

2. the cross-scale fine analysis method

2.1. Scaled boundary finite element analysis method

In recent years, significant advancements have been made in the development of the scaled boundary finite element method (SBFEM), leading to rapid growth and substantial research contributions. It has addressed numerous scientific challenges (Natarajan et al., 2020; Natarajan and Song, 2013; Li et al., 2023). This section primarily introduces the theory of polygonal SBFEM element. By using the boundary discretization and radial analytical method, the arbitrary polygon interpolation function Φ and strain displacement matrix B can be directly obtained. These formulas are provided in Eq. (1) and (2).

$$\Phi(\xi, s) = N_u(s)\psi_u \xi^{-s_n} \psi_u^{-1} \quad (1)$$

$$B(\xi, s) = [B_1(s)\psi[-S_n] + B_2(s)\psi] \xi^{-s_n-1} \psi_u^{-1} \quad (2)$$

Through the integration points in the domain, the polygonal element stiffness matrix can be obtained. This formula is listed in Eq. (3).

$$K_{ep} = \sum_{i=1}^{3n} B^i(\xi, s) D_{ep}^i B^i(\xi, s) A_i \quad (3)$$

By bringing in relevant variables, the internal and external force vectors can be solved. These formulas are listed in Eq. (4) to (8).

$$R_{ext} = \int_{\Gamma} \Phi^T(\xi, s) f_1 d\Gamma + \int_{\Omega} \Phi^T(\xi, s) f_b d\Omega \quad (4)$$

$$\int_{\Gamma} \Phi^T(\xi, s) f_1 d\Gamma = \int_{-1}^1 N_u(s) |J(s)| f_1 ds \quad (5)$$

$$\int_{\Omega} \Phi^T(\xi, s) f_b d\Omega = \sum_{k=1}^n \sum_{i=1}^3 [N_u^i(s) \psi_u \xi_i^{-s_n} \psi_u^{-1}]^T f_b A_{ki} \quad (6)$$

$$R_{\text{int}} = \sum_{i=1}^{3n} B^i(\xi, s)^T \sigma_i(\xi, s) A_i \quad (7)$$

$$\sigma_i(\xi, s) = \sum_{j=1}^{3n} D_{\text{ep}}^i \varepsilon_j(\xi, s) \quad (8)$$

The numerical solution in the computational domain can be obtained by iteratively solving the mechanical equilibrium equation. This formula is listed in Eq. (9). For detailed derivation and implementation process, please refer to the literature (Wolf and Song, 2001).

$$\left(\sum_{i=1}^{n_{\text{Pol}}} K_{\text{ep}} \right) \Delta U_b = \sum_{i=1}^{n_{\text{Pol}}} (R_{\text{ext}} - R_{\text{int}}) \quad (9)$$

2.2. Analysis platform

GEODYNA is utilized for the calculation. GEODYNA is a sophisticated geotechnical analysis software developed independently by Dalian University of Technology (Degao et al., 2005). Multicore parallel technology is used in this program to provide computing power and solve large-scale elastic-plastic analysis problems involving millions of degrees of freedom (Chen et al., 2024; Qu et al., 2021; Zou et al., 2019). On this platform, polygonal scaled boundary finite element method (SBFEM) elements have been integrated. Additionally, programs for viscoelastic boundary conditions, polygonal interface elements, polyhedral preprocessing visualization, and editing and modification have been developed, thereby enhancing the flexibility and versatility of traditional analysis methods. Coupled analysis of SBFEM-FEM can be performed, and the software is compatible with all commonly used constitutive models for dam materials.

3. Static and dynamic calculation results and analysis of anti-seepage joint

3.1. Cross-scale fine computing model

The hybrid dam primarily consists of concrete gravity dam, asphalt concrete anti-seepage panel, rockfill and bedrock, as illustrated in Fig. 1. The concrete gravity dam has slopes of 1:1.3 and 0.9:1. The dam is 85 m high, with a top width of 10 m and a bottom width of 80 m. The asphalt concrete anti-seepage panel has a thickness of 0.2 m, with joints thickened to 0.5 m. Beneath the panel, the rockfill is arranged in a “V”-shape. The maximum filling depth of the “V”-shaped rockfill area I is 25 m, while for rockfill area II, it is 28 m. The rockfill was filled in 32 steps. The

reservoir’s water storage height is 40 m, and it’s stored in 14 steps.

The aim of this paper is to investigate the dislocation deformation of the panel at the anti-seepage joint under the influence of water storage pressure and dynamic load. To achieve this, the joint has been refined into a mesh, as depicted in Fig. 2. The mesh within the joint has been densified to enhance accuracy. To minimize model discretization errors and ensure geometric precision, a hybrid element comprising of quadrilateral and proportional boundary polygons has been generated at the structural interface. Grid density is appropriately reduced at the bedrock. The interface between the rockfill, gravity dam, and asphalt panel is simulated using Goodman contact elements. The slip displacement at the interface is expressed by the deformation of the contact element. The final model comprises a total of 7797 elements and 8303 nodes.

3.2. Constitutive model and calculation parameters

The equivalent linear model based on nonlinear elastic theory is commonly employed for analyzing the weakly nonlinear dynamic response of hydraulic structures under seismic loading. However, it is difficult for the equivalent linear analysis method to reflect the actual situation for strong nonlinear states. To address this limitation and accurately reflect the strong nonlinear properties of reservoir. The generalized plastic model (Liu et al., 2018; Zou et al., 2013) is utilized in this analysis to simulate the cushion, rockfill, and asphalt panel. Detailed parameters are provided in Tables 1-2. The linear elastic model is applied to simulate the gravity dam and bedrock, with parameters detailed in Table 3. Additionally, the generalized plastic contact surface model (Liu et al., 2015) is employed to simulate the contact surfaces between various structures, as outlined in Table 4.

3.3. Seismic input

The seismic input for the hybrid dam is based on the standard spectrum seismic wave, with peak horizontal and vertical seismic accelerations set at 0.45 g. The seismic wave acceleration time history is depicted in Fig. 3. The duration of the seismic wave used in the calculation is 30 s. To account for the interaction between the dam and the foundation, an artificial boundary and equivalent load-based wave input method are employed.

3.4. Static result analysis

3.4.1. Deformation analysis of anti-seepage joint

In this paper, vertical downward deformation is defined as a negative value in the y-direction, while horizontal deformation directed towards the gravity dam is defined as a negative value in the x-direction. These definitions are reversed for all other cases. Fig. 4 shows the local and

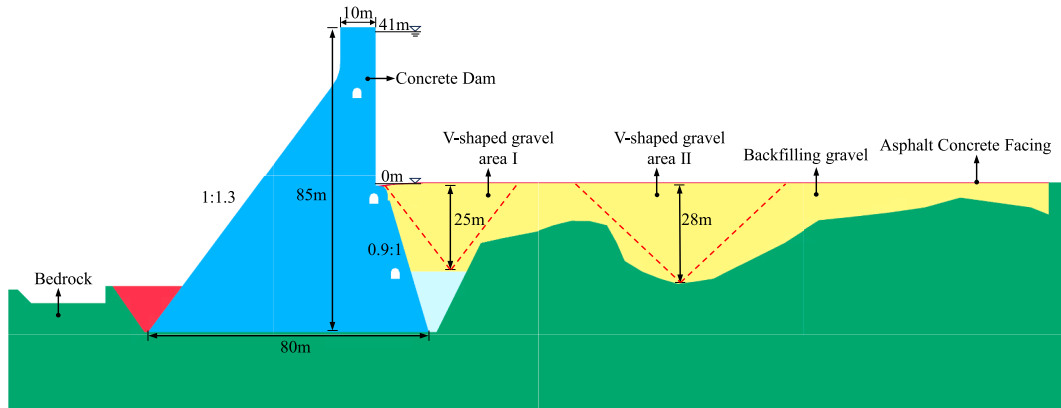


Fig. 1. Two-dimensional model of mixed dam reservoirs.

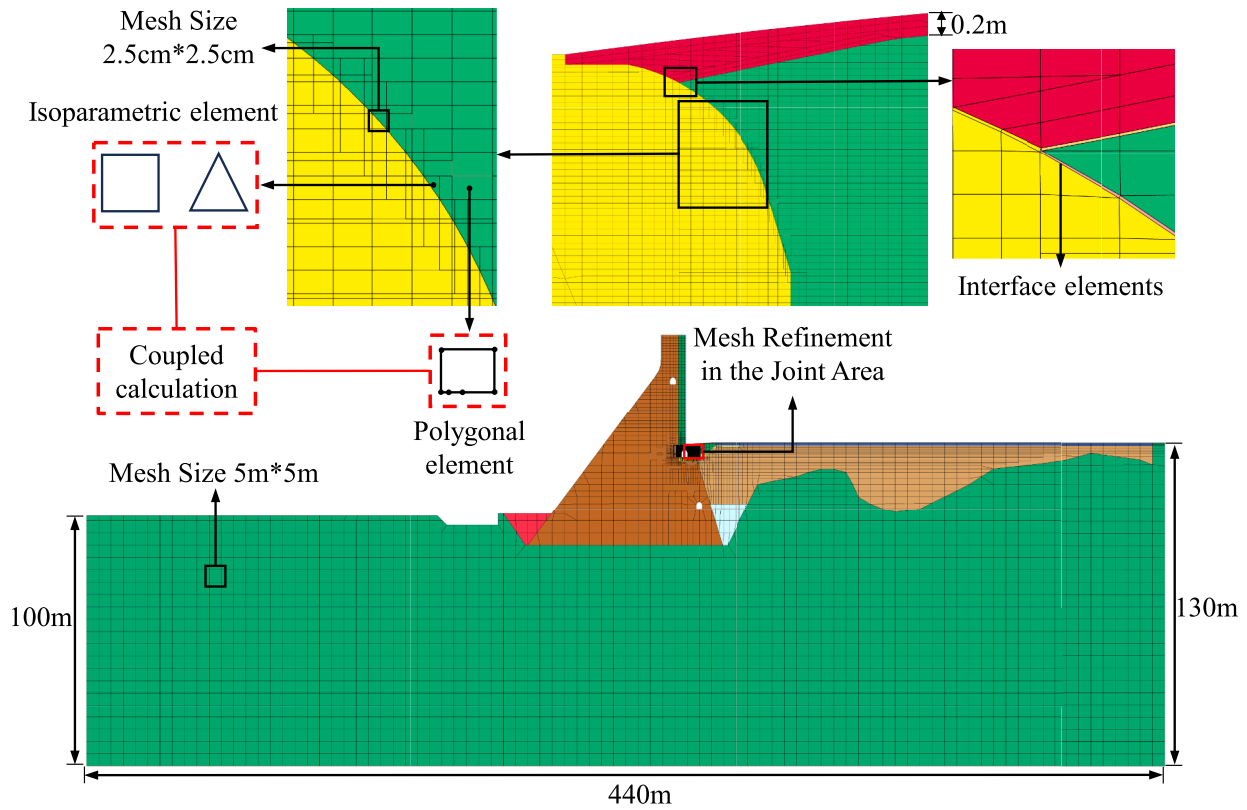


Fig. 2. Cross scale grid model.

Table 1
Generalized plastic model parameters.

Material	G_0	K_0	M_g	M_f	α_f	α_g	H_0	H_{U0}	m_s
Asphalt panel	5120	4,809	1.67	1.15	0.1	-0.9	500	500	0.155
Backfilling gravel	710	949	1.72	1.2	0.2	0.3	600	3600	0.3
Cushion	1543	1339	1.69	1.20	0.25	0.45	600	1000	0.4

Table 2
Generalized plastic model parameters.

Material	m_v	m_l	m_u	r_d	γ_{DM}	γ_u	β_0	β_1
Asphalt panel	0.155	0.1	0.19	100	100	10	10	0.02
Backfilling gravel	0.3	0.2	0.2	3	10	7	20	0.02
Cushion	0.4	0.31	0.31	3	12	3.8	40	0.028

Table 3
Parameters of linear elastic material.

Material	E/MPa	μ
Bedrock	10,000	0.25
Gravity dam	25,500	0.167

overall deformation results of the hybrid dam when fully impounded. It is evident from Fig. 4 that the deformation of the asphalt panel is coordinated with the deformation of the rockfill. Due to the differences in

initial modulus, there is a significant disparity in deformation between the rockfill and the concrete dam. While the rockfill exhibits substantial deformation, the concrete dam remains relatively stable. The maximum settlement value of 18.0 cm is observed at the center of the V-shaped rockfill area, with the value decreasing gradually towards both sides. The settlement value decreases gradually from the center towards both sides. Following foundation settlement deformation, the two sides of the V-shaped rockfill area exhibit horizontal deformation directed towards the center, with a maximum displacement of 3.3 cm. Significant deformation is observed at both sides of the overlapping area between the asphalt panel and the concrete dam. The settlement values show considerable variation, ranging from less than 2.0 cm at the joint to over 15.0 cm at the center of the V-shaped rockfill area. The horizontal deformation exhibits only minor changes, with the deformation consistently pointing towards the center of the V-shaped rockfill area. On the right side of the joint, horizontal deformation initially increases and then decreases, with the maximum horizontal deformation reaching 33.0 cm and the minimum value at 1.0 cm.

Table 4
Parameters of the generalized plastic interface model.

Elastic modulus		Critical state			Plastic direction		Plastic modulus			Loading direction	
D_{s0}	D_{n0}	M_c	e_{r0}	λ	α	r_d	k	H_0	f_h	k_m	M_f
1000	4500	0.66	0.4	0.091	0.65	0.2	0.5	8500	2	0.6	0.65

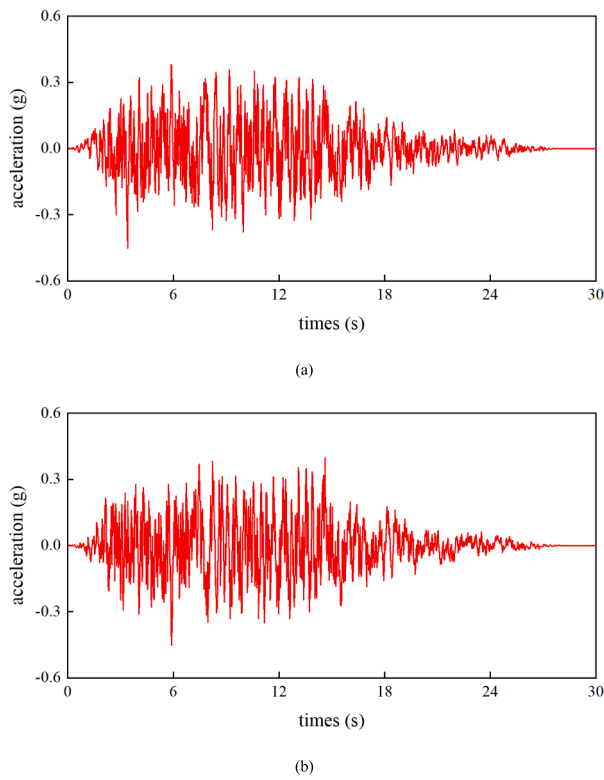


Fig. 3. Input acceleration records: (a)x-direction, (b)y-direction.

3.4.2. Slip analysis of panel overlap area

Fig. 5 depicts the slip envelope at Interface I (the interface between asphalt panel and concrete dam) and Interface II (the interface between rockfill and concrete dam) during full storage. Point A represents the intersection of the two interfaces. As can be seen from Fig. 5, the slip amount on Interface I increases gradually with the extension of the interface, while the slip amount on Interface II initially increases and then decreases with the extension of the interface. The amount of slip below interface point A is significantly greater than that above it. The slip amount at interface point A is 1.2 cm, and the maximum slip amount near the joint is located below interface point A, with a maximum value of 3.29 cm.

Fig. 6 depicts the slip displacement at the junction point A during the reservoir impoundment process. According to Fig. 6, the slip amount at junction point A is minimized when the water level is at 0 m, measuring at 0.17 cm. The slip amount at junction point A increases continuously

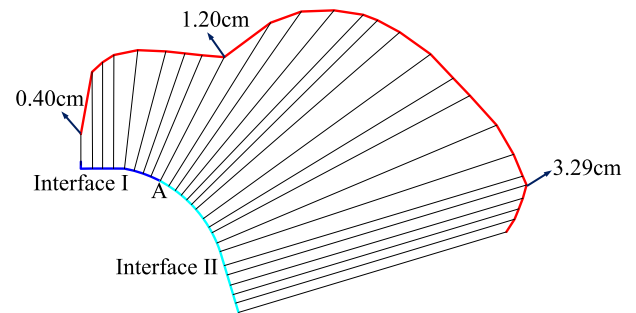


Fig. 5. Dislocation momentum on the interface after water storage.

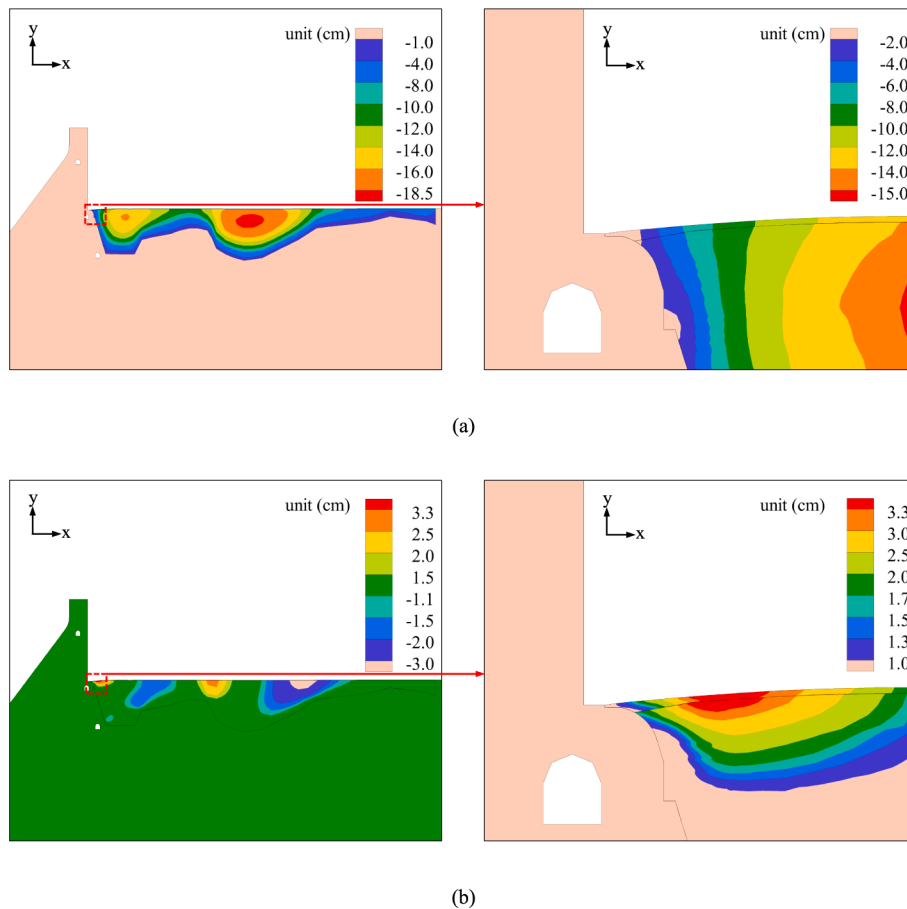


Fig. 4. Deformation of mixed dam after water storage: (a) vertical settlement, (b) horizontal deformation.

as the water level rises. At full water level, the slip reaches a maximum value of 1.2 cm.

3.4.3. Strain analysis of anti-seepage joint

Fig. 7 shows the horizontal tensile strain and vertical compressive strain of the panel in the anti-seepage joint when fully impounded. Asphalt concrete materials exhibit good compressive properties but poor tensile properties. When the tensile strain is large, the asphalt concrete will crack and become damaged. Therefore, it is important to consider the tensile strain value of the panel to prevent damage to the anti-seepage panel. According to the laboratory test results and engineering data, the design value for panel tensile strain should be less than 1.0 %. As can be seen from Fig. 7(a), the panel in the anti-seepage joint exhibits a relatively large tensile strain value. The maximum tensile strain value is 0.91 %. The weak area is located on the upper right side of junction A. As illustrated in Fig. 7(b), the anti-seepage joint has a maximum compressive strain of 0.85 %, providing ample safety margin.

3.5. Dynamic result analysis

3.5.1. Deformation analysis of anti-seepage joint

Fig. 8 shows the local and overall deformation results of the hybrid dam under dynamic load. As depicted in Fig. 8, the deformation laws for both overall and local structures under dynamic load are identical to those under static load. The deformation of the asphalt panel and rockfill material is well-coordinated. Due to differences in initial modulus, the concrete dam and rockfill occurs significant uneven deformation. The rockfill deformed significantly, while the concrete dam deformed minimally. The maximum settlement value in the rockfill area is 5.5 cm, and the maximum horizontal deformation value is 1.5 cm. The maximum settlement value in the anti-seepage joint is 4.9 cm, and the maximum horizontal deformation value is 1.4 cm.

3.5.2. Slip analysis of panel overlap area

Fig. 9 shows the slip envelope of the Interface I and Interface II under dynamic load. The displacement of the structure under dynamic loads follows the same law as that under static loads. The slip amount on Interface I increases gradually as the interface extends, while the slip amount on Interface II initially increases and then decreases with extension. The slip amount on the Interfaces I and II increases significantly under dynamic load. The slip distance at the junction point A is 3.17 cm, and the maximum slip distance on the Interface II is 4.77 cm.

Fig. 10 depicts the slip time-history curve at the junction point A under dynamic load. Fig. 10 illustrates that the slip at junction point A exhibited a fluctuating growth trend during the early to mid-stage of the earthquake, and stabilized at approximately 3.1 cm during the late stage of the earthquake without significant changes. This is primarily because

the rockfill undergoes permanent deformation under dynamic loads. During the initial and intermediate stages of the earthquake, the significant increase in seismic acceleration results in a rapid increase in displacement at the interface.

3.5.3. Strain analysis of anti-seepage joint

According to the laboratory test results and engineering data, the design value for panel tensile strain should not exceed 3.0 %. Fig. 11 shows the horizontal tensile strain and vertical compressive strain of the anti-seepage joint panel under dynamic load. It can be seen from Fig. 11 (a) that the panel in the anti-seepage joint has a relatively large tensile strain value. Compared to the static condition, the panel only has one weak area located at the upper left junction point A, with a maximum tensile strain of 1.21 %. After analyzing the tensile strain results of the panel under both static and dynamic conditions, it was determined that the weak area of the anti-seepage panel is located on the upper right side of junction A. Therefore, additional attention should be paid to its tensile strain value. From Fig. 11(b), it is observed that the panel at the anti-seepage joint experiences a maximum compressive strain of 1.05 %, indicating a sufficient safety margin against compression.

4. Calculation results and analysis of step-type anti-slip and anti-seepage design

The analysis results from the previous section indicate that the weak area of the anti-seepage system is located at the joint of the anti-seepage panel. Due to the uneven settlement of the rockfill and concrete structures, the asphalt panel and rockfill in the anti-seepage joint experience slippage along the concrete lap platform, resulting in significant horizontal tensile strains at the top of the asphalt panel. To address these issues, a step-type design scheme has been proposed based on the characteristics of the weak area and the deformation behavior of the anti-seepage panel.

4.1. Step-type anti-slip and anti-seepage design scheme

As shown in Fig. 12, the stepped optimization design mainly consists of three forms. For the location of the weak area, the stepped layout range is located below the interface junction point A.

1) single-step form

The step height is a variable that is divided into seven condition groups for the single-step form, as detailed in Table 5. This study aims to investigate the mechanisms and impacts of the single-step reinforcement scheme at varying reinforcement depths.

2) multiple steps discontinuous form

The height of each individual step is either 0.075 m or 0.015 m when using the multi-step discontinuous form for reinforcement. The working conditions are categorized into eight groups based on the reinforcement depth, as detailed in Table 6. This study explores the mechanisms and effects of multiple-step reinforcement schemes at varying reinforcement depths.

3) multiple steps continuous form

When using the continuous form for reinforcement with multiple steps, the reinforcement depth should remain constant at 0.45 m, while the step height varies. The working conditions are categorized into four groups, as detailed in Table 7. This study aims to investigate the impact of step size and spacing on the effectiveness of reinforcement schemes from various perspectives.

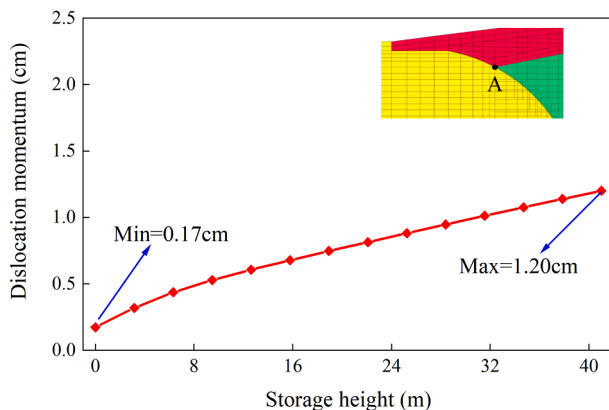


Fig. 6. Time history curve of displacement at the intersection point A after water storage.

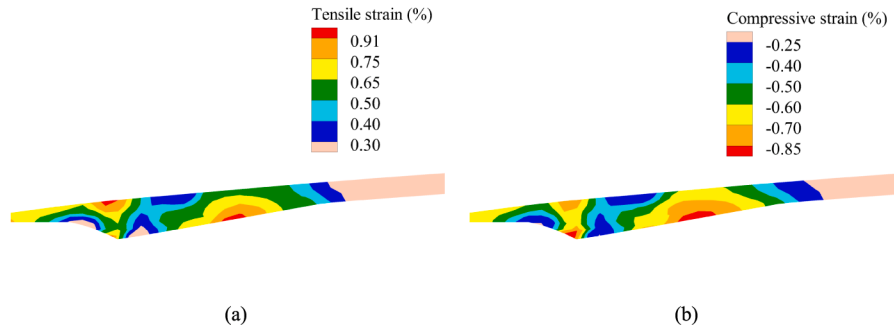


Fig. 7. The strain of panel after water storage: (a) Horizontal tensile strain, (b) Vertical compressive strain.

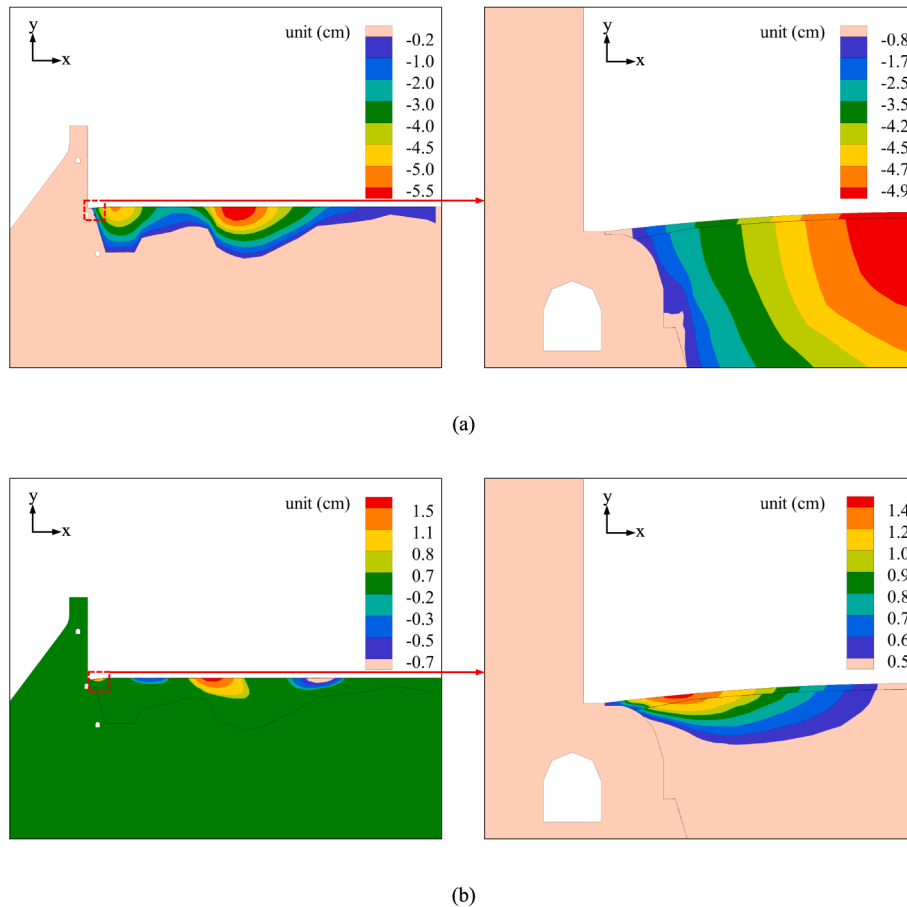


Fig. 8. Deformation of mixed dam under dynamic load: (a) vertical settlement, (b) horizontal deformation.

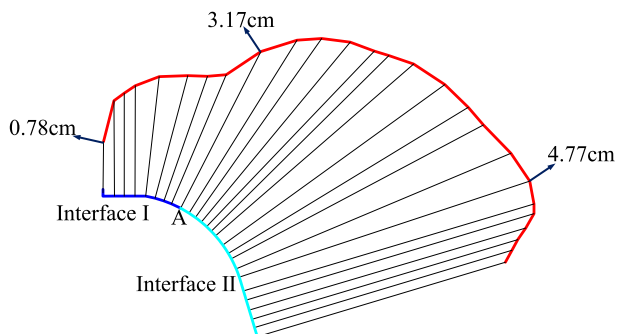


Fig. 9. Dislocation momentum on the interface under dynamic load.

4.2. Static result analysis

4.2.1. Single-step form

Fig. 13 depicts the panel strain and interface sliding in the anti-seepage joint when reinforced using a single-step form. It can be seen from Fig. 13 that the optimization effect on panel tensile strain and interface slippage is minimal with smaller step heights. The effectiveness of optimization improves progressively with increasing step height. For step heights of 0.375 m and 0.45 m, the maximum tensile strain of the panel decreases to 0.79 % and 0.80 %, respectively. With step heights of 0.375 m and 0.45 m, the maximum tensile strain of the panel decreases to 0.79 % and 0.80 %, respectively, with optimization rates increasing by 13.0 % and 12.0 %, respectively. Additionally, the maximum interface slip decreases to 2.88 cm and 2.85 cm, respectively, with optimization rates improving by 12.46 % and 13.37 %, respectively.

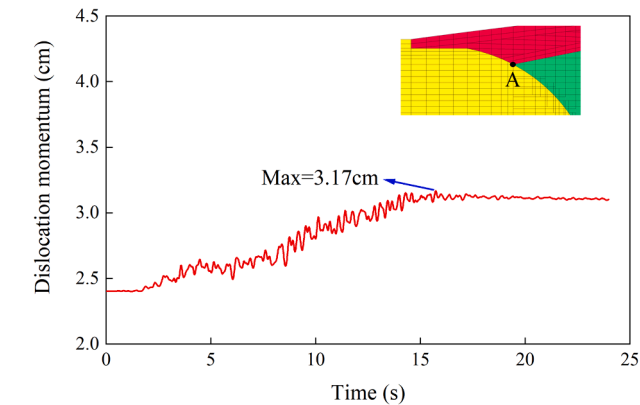


Fig. 10. Time history curve of displacement at junction A under dynamic load.

Figs. 14–16 respectively show the horizontal deformation, vertical settlement and panel strain of the joint when using $h = 0.6$ m, 0.45 m step reinforcement and no reinforcement. Fig. 14 and Fig. 15 illustrate that both horizontal deformation and vertical settlement at the joint are significantly reduced with step reinforcement. Fig. 16 reveals that with $h = 0.45$ m step reinforcement, the weak point shifts to the right, and the maximum tensile strain decreases by 12.0 % compared to the unreinforced condition. Conversely, for $h = 0.6$ m step reinforcement, the weak point also shifts to the right, but the maximum tensile strain increases by 3.0 % compared to the unreinforced condition. It is observed that the rate of interface slip, horizontal deformation, and vertical settlement increase with step height. However, excessive reduction of interfacial slip and panel deformation due to larger step heights results in increased deformation gradient and higher tensile strain values at weaker areas. It is recommended to control the step height within the range of 0.375 to

0.45 m.

4.2.2. Multiple steps discontinuous form

Fig. 17 and Fig. 18 illustrate the tensile strain and interface sliding amount of the panel in the anti-seepage joint when reinforced using a multistep discontinuous form. From Fig. 17, it can be observed that as the number of steps increases, the tensile strain of the panel initially decreases and then increases, while the interface slip continues to decrease. The optimal reinforcement depth is $H=0.525$ m, where the tensile strain of the panel is 0.86 %, resulting in a 5.0 % improvement, and the interface sliding amount is 2.79 cm, showing a 15.2 % reduction. Fig. 18 indicates that as the reinforcement depth increases, the tensile strain of the panel decreases initially and then increases, with the interface slippage continually decreasing. The optimal reinforcement depth is $H=0.45$ m. The panel’s tensile strain is 0.80 %, with an optimization rate of 12.0 %. The interfacial sliding amount is 2.82 cm, with an optimization rate of 14.29 %.

Figs. 19–21 respectively show the horizontal deformation, vertical settlement and panel strain of the joint when reinforced in a multiple step discontinuous form. As observed from Figs. 19–21, excessive reduction in horizontal deformation and vertical settlement in the joint has resulted in a shift of the weak areas of the panels to the right.

Table 5

The cases of single step.

Case	1	2	3	4	5	6	7
Step height	0.075	0.15	0.3	0.375	0.45	0.525	0.6
	m	m	m	m	m	m	m
Number of steps	1	1	1	1	1	1	1
Step spacing	0 m	0 m	0 m	0 m	0 m	0 m	0 m
Reinforcement depth	0.075	0.15	0.3	0.375	0.45	0.525	0.6
	m	m	m	m	m	m	m

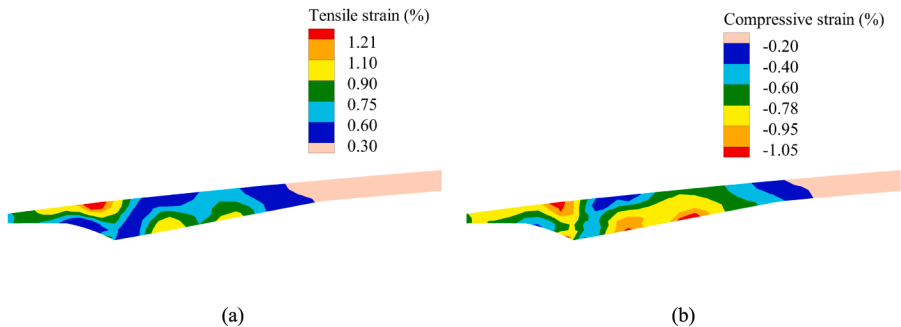


Fig. 11. The strain of panel in the joint: (a) Horizontal tensile strain, (b) Vertical compressive strain.

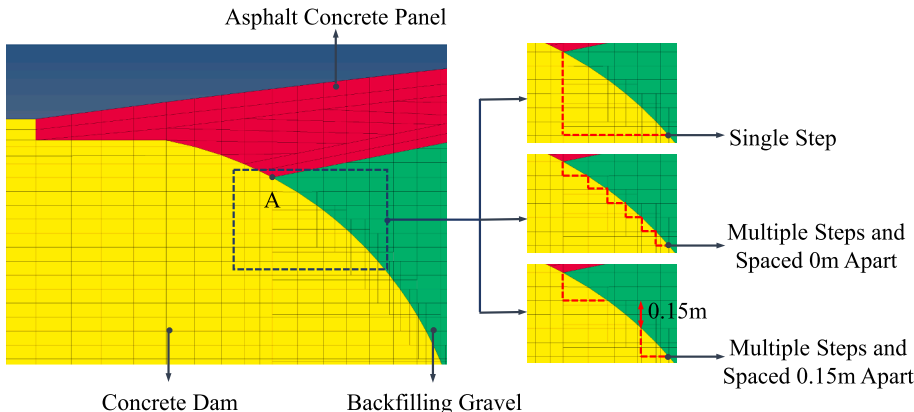


Fig. 12. The layout form of step style anti-slip design.

Table 6

The cases of multiple steps.

Case	8	9	10	11	12	13	14	15
Step height	0.075 m	0.075 m	0.075 m	0.075 m	0.15 m	0.15 m	0.15 m	0.15 m
Number of steps	1	2	3	4	1	2	3	3
Step spacing	0 m	0.15 m	0.15 m	0.15 m	0 m	0.15 m	0.075 m	0.15 m
Reinforcement depth	0.075 m	0.3 m	0.525 m	0.75 m	0.15 m	0.45 m	0.6 m	0.75 m

Table 7

The cases of multiple steps.

Case	16	17	18	19
Step height	0.45 m	0.15 m	0.15 m	0.075 m
Number of steps	1	2	3	6
Step spacing	0 m	0.15 m	0 m	0 m
Reinforcement depth	0.45 m	0.45 m	0.45 m	0.45 m

Notably, weak areas with larger tensile strain values appear at $H=0.75$ m. The maximum tensile strain of the panels after reinforcement with a step height of $h = 0.15$ m increased by 10.0 % compared to the unreinforced condition. Similarly, the maximum tensile strain of the panels after reinforcement with a step height of $h = 0.075$ m increased by 4.0 % compared to the unreinforced condition. This indicates that excessive reinforcement depth leads to an increased deformation gradient of the panel, resulting in weak areas with higher tensile strain values. To achieve optimal reinforcement, the reinforcing depth should be controlled at approximately 0.45 m.

4.2.3. Multiple steps continuous form

Fig. 22 depicts the maximum tensile strain and interface sliding

amount of the panel in the anti-seepage joint when multiple steps continuous reinforcement is applied. As shown in Fig. 16, the optimization rate for interface slippage is approximately 14.0 % at a reinforcement depth of 0.45 m. In Case 19, with a step height of 0.075 m, the panel tensile strain optimization rate is 7.0 %. For step heights of 0.15 m and 0.45 m in Cases 18 and 16, respectively, the panel tensile strain optimization rates are 11.0 % and 12.0 %. This indicates that a step height of no less than 0.075 m is required to achieve superior reinforcement effects under static load. Case 17 has a step height and spacing of 0.15 m. The optimized tensile strain of the panel is about 12.0 %, offering improved reinforcement compared to Case 18. Therefore, increasing the step spacing accordingly results in improved reinforcing effects.

4.3. Dynamic result analysis

4.3.1. Single-step form

Fig. 23 depicts the tensile strain and interface sliding amount of the panel in the anti-seepage joint when reinforced using a single-step form under dynamic load. As shown in Fig. 23, the optimization rate for panel tensile strain exhibits a decreasing trend as the step height increases, while the optimization rate for interface slip first increases and then

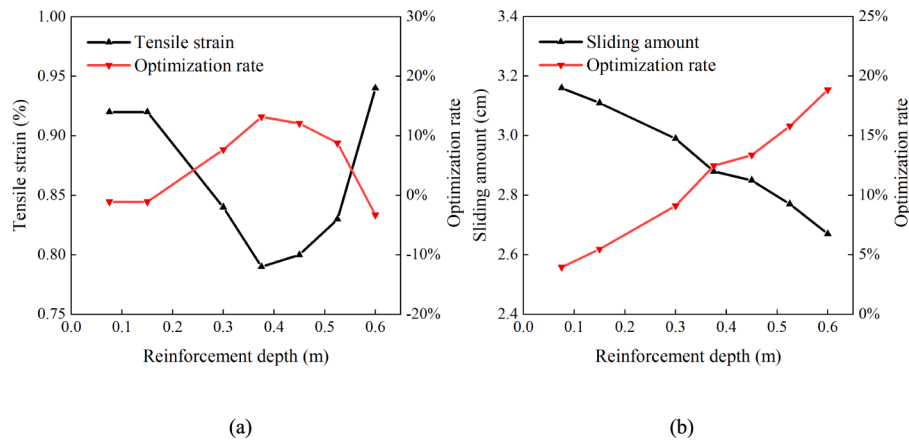


Fig. 13. Deformation of panel joints reinforced by single step: (a) Maximum tensile strain, and (b) Dislocation momentum.

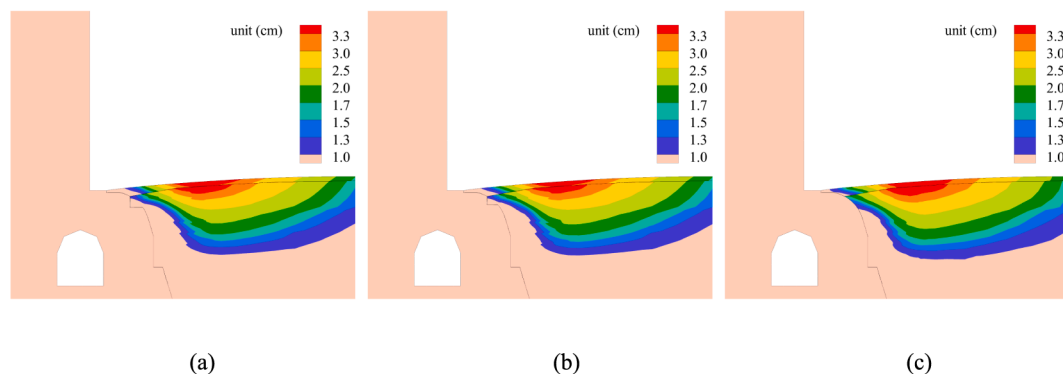


Fig. 14. Horizontal deformation of the joint: (a) $h = 0.6$ m, (b) $h = 0.45$ m, (c) unreinforced.

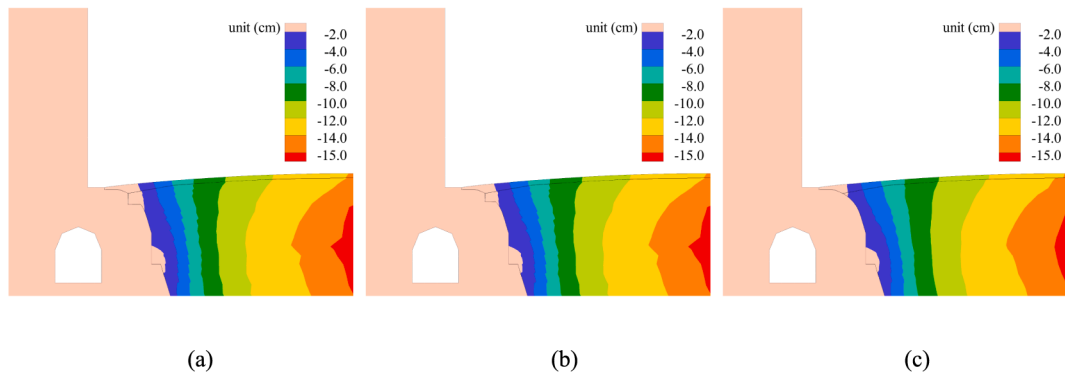


Fig. 15. Vertical settlement of the joint: (a) $h = 0.6$ m, (b) $h = 0.45$ m, (c) unreinforced.

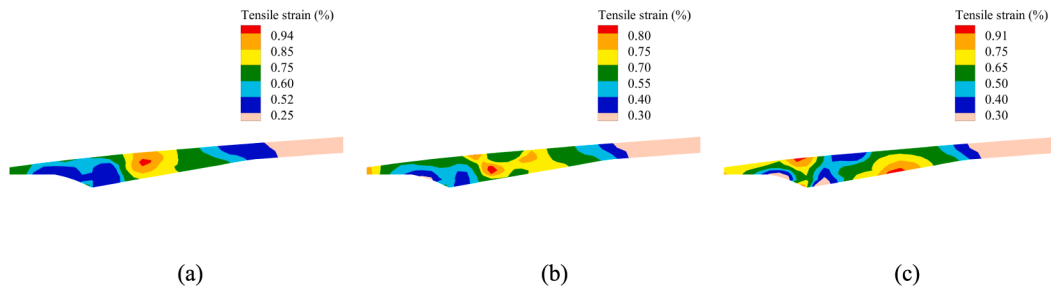


Fig. 16. Panel strain of the joint: (a) $h = 0.6$ m, (b) $h = 0.45$ m, (c) unreinforced.

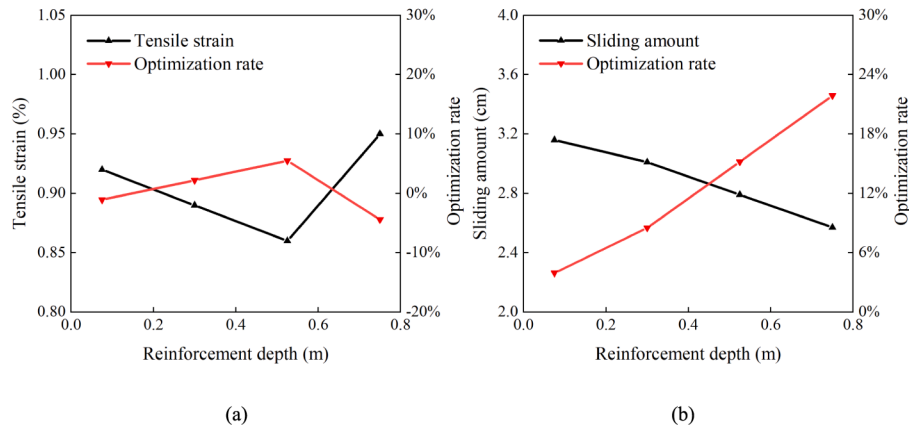


Fig. 17. Deformation of panel joints reinforced by multiple steps ($h = 0.075$ m): (a) Maximum tensile strain and (b) Dislocation momentum.

decreases. At a step height of 0.15 m, the optimization rate for panel tensile strain compared to interface slip is approximately 7.0 %. However, the panel tensile strain increases to 1.43 % when the step height is raised to 0.6 m.

Figs. 24–26 respectively show the horizontal deformation, vertical settlement, and panel strain of the joint with reinforcement heights of $h = 0.6$ m, 0.45 m, and no reinforcement. As depicted in Fig. 24 and Fig. 25, the horizontal deformation of the joint is significantly reduced with step-type reinforcement. The vertical settlement changes relatively little after applying the step-type reinforcement. The weak area of the panel was notably shifted and the tensile strain increased by 13.0 % with $h = 0.6$ m reinforcement. Although the weak area of the panel also shifted to the right with $h = 0.45$ m reinforcement, the maximum tensile strain value remained unchanged.

4.3.2. Multiple steps discontinuous form

Fig. 27 and Fig. 28 depict the panel tensile strain and interfacial

sliding in the anti-seepage joint when reinforced using multiple steps under dynamic load. It can be observed from Fig. 27 and Fig. 28 that the optimized panel tensile strain rate decreases, while the optimized interfacial slip rate increases with the height of the steps. The optimization rates for panel tensile strain are 7.43 % and 4.13 %, and for interfacial slip are 17.19 % and 9.64 % at reinforcement depths of 0.45 m and 0.3 m, respectively.

Figs. 29–31 show the horizontal deformation, vertical settlement, and panel strain of the joint after reinforcement respectively and without reinforcement under dynamic load. The results indicate that the weak point shifts to the right and the tensile strain values increase in the anti-seepage panel when the reinforcement depth is $H=0.75$ m. Therefore, the depth of reinforcement should be controlled to around 0.45 m when using multiple step schemes for reinforcement.

4.3.3. Multiple steps continuous form

Fig. 32 depicts the panel tensile strain and interfacial sliding in the

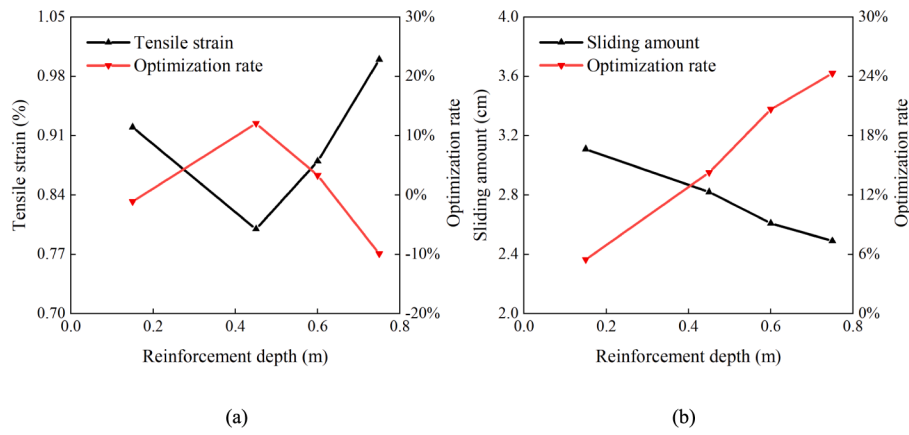


Fig. 18. Deformation of panel joints reinforced by multiple steps ($h = 0.15$ m): (a) Maximum tensile strain and (b) Dislocation momentum.

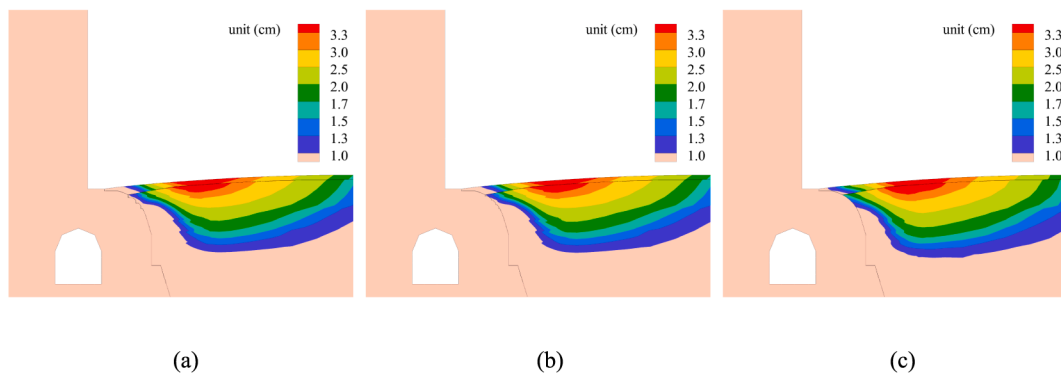


Fig. 19. Horizontal deformation of the joint: (a) $h = 0.15$ m, $H = 0.75$ m, (b) $h = 0.075$ m, $H = 0.75$ m, (c) unreinforced.

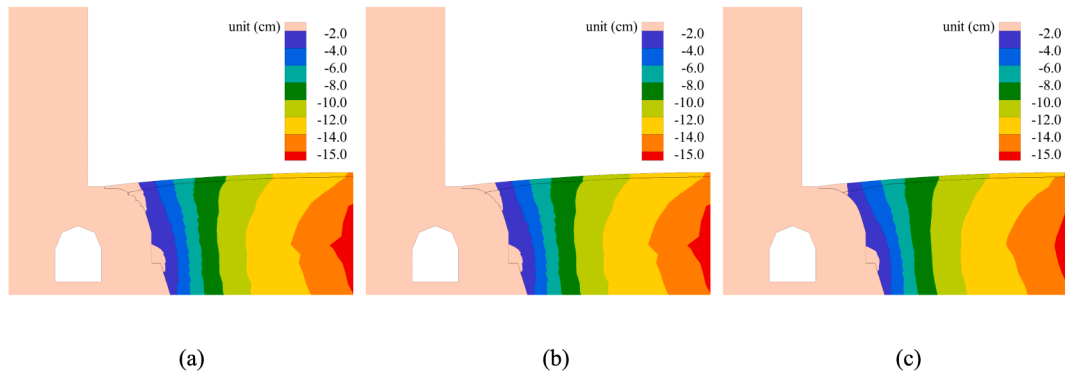


Fig. 20. Vertical settlement of the joint: (a) $h = 0.15$ m, $H = 0.75$ m, (b) $h = 0.075$ m, $H = 0.75$ m, (c) unreinforced.

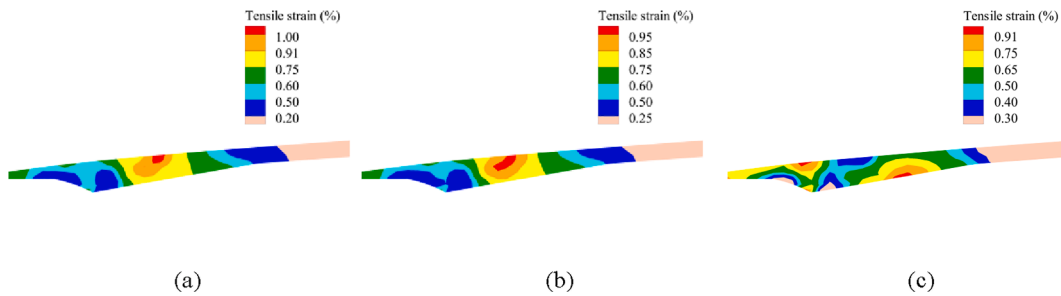


Fig. 21. Panel strain of the joint: (a) $h = 0.15$ m, $H = 0.75$ m, (b) $h = 0.075$ m, $H = 0.75$ m, (c) unreinforced.

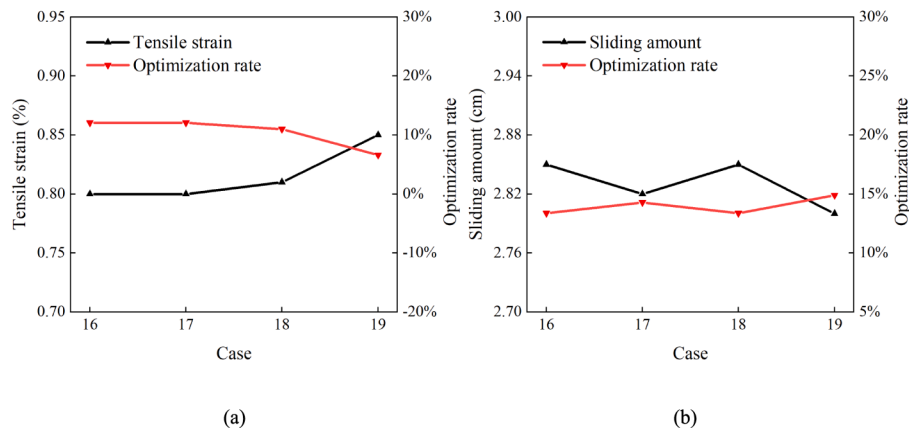


Fig. 22. Deformation of panel joints reinforced by multiple steps under dynamic load: (a) Maximum tensile strain and (b) Dislocation momentum.

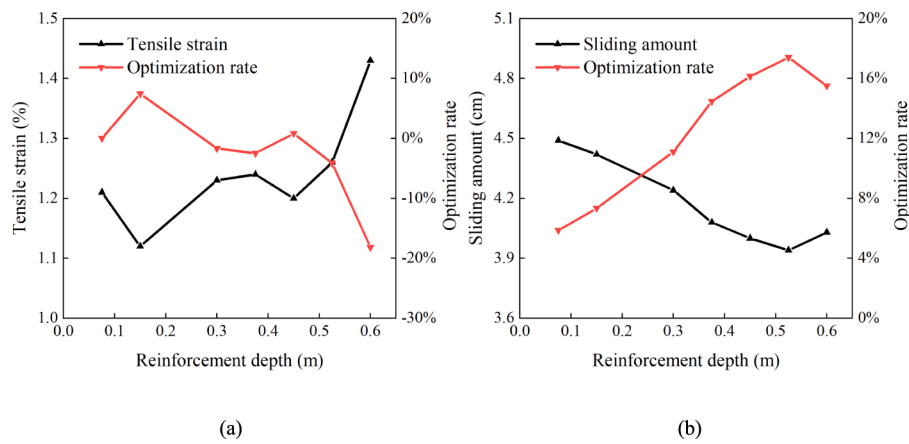


Fig. 23. Deformation of panel joints reinforced by single step under dynamic load: (a) Maximum tensile strain and (b) Dislocation momentum.

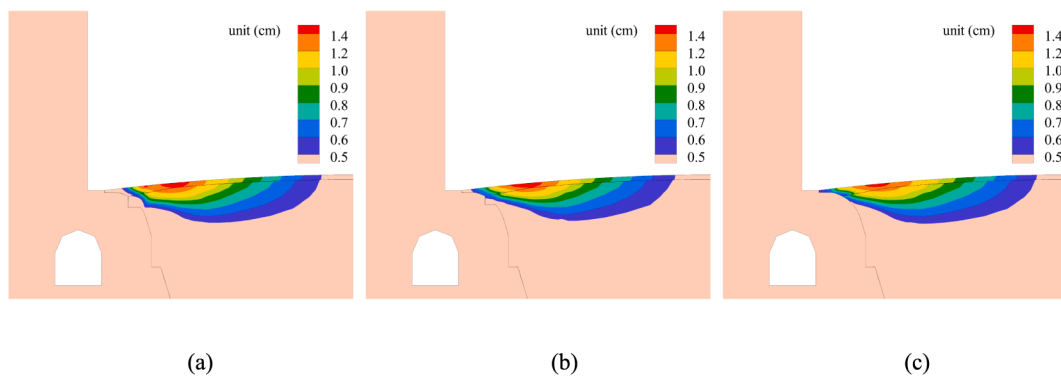


Fig. 24. Horizontal deformation of the joint under dynamic load: (a) $h = 0.6$ m, (b) $h = 0.45$ m, (c) unreinforced.

anti-seepage joint when reinforced using multiple steps under dynamic load. As shown in Fig. 32, the optimization rate for interfacial slip is approximately 16.5 % at a reinforcement depth of 0.45 m. The tensile strain of the panel increases by 4.0 % when the step height is 0.075 m. Therefore, the height of the steps should not be less than 0.075 m when employing the step reinforcement scheme. Additionally, increasing the spacing between the steps can further optimize the reinforcing effect.

5. Conclusions

The deformation characteristics of a typical dam under static and

dynamic conditions were investigated using the cross-scale approach and the scaled boundary finite element method (SBFEM). And the weak area in the anti-seepage system has been identified. Based on simulations, a fresh step-type design was proposed to enhance the stability performance of the anti-seepage joint. The mechanisms and effects of the step-type design are discussed from various perspectives through simulations. The main conclusions are as follows:

- (1) Under the action of water storage pressure and seismic load, the deformation of anti-seepage panel and rockfill is coordinated. However, the settlement of concrete dam and rockfill dam is

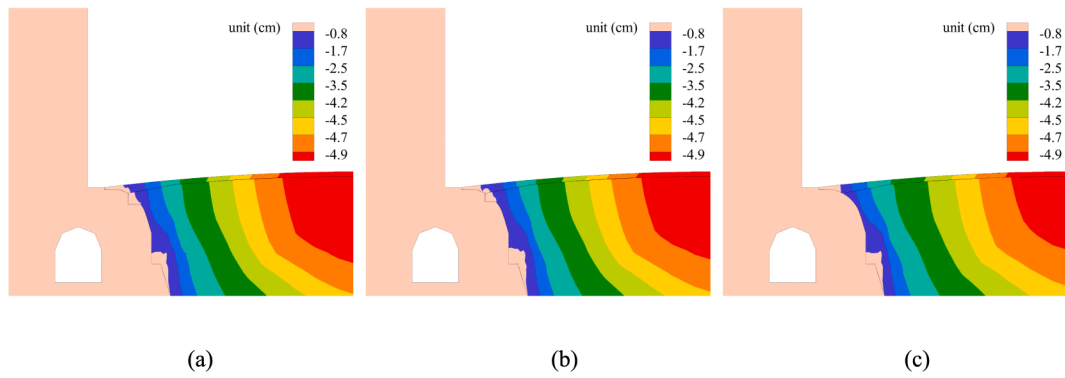


Fig. 25. Vertical settlement of the joint under dynamic load: (a) $h = 0.6$ m, (b) $h = 0.45$ m, (c) unreinforced.

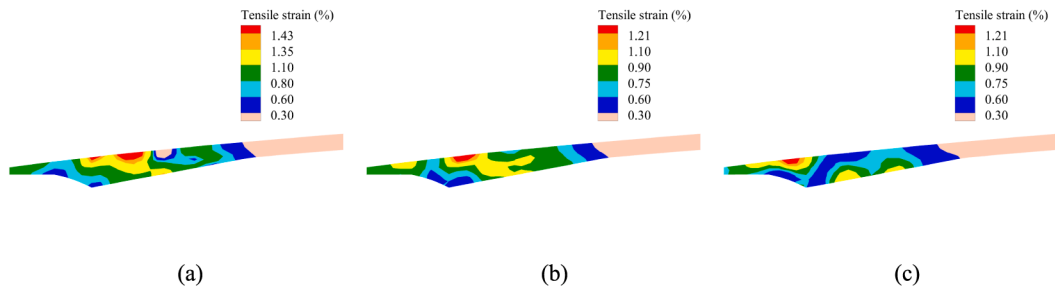


Fig. 26. Panel strain of the joint under dynamic load: (a) $h = 0.6$ m, (b) $h = 0.45$ m, (c) unreinforced.

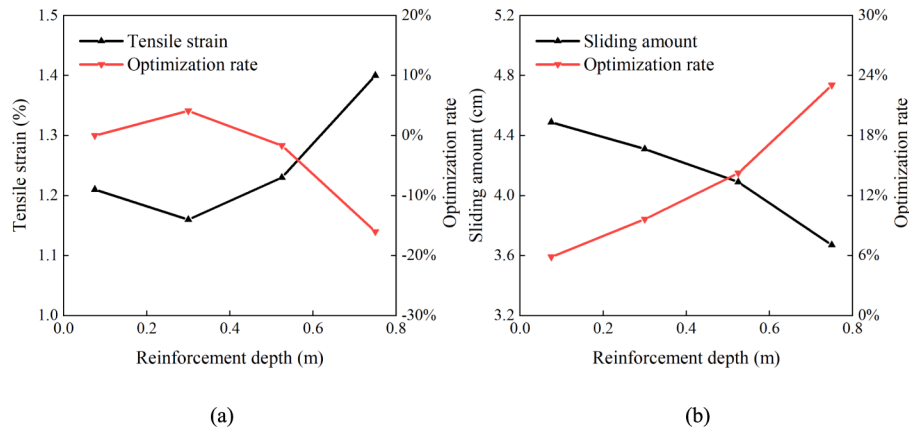


Fig. 27. Deformation of panel joints reinforced by multiple steps ($h = 0.075$ m) under dynamic load: (a) Maximum tensile strain and (b) Dislocation momentum.

- uneven. And the uneven deformation resulting in the asphalt panel slide along the underlying lapped concrete platform, meanwhile, significant horizontal tensile strain will emerge on the top of the panel. Consequently, the anti-seepage joint could be identified as the weak area of the reservoir anti-seepage system.
- (2) A positive reinforcement effect was provided by the step-type design. It notably reduced the slipping displacements along the interface and the tensile strain in the asphalt panel by hindering the slip path of the rockfill. However, excessive reduction in sliding could increase the settlement gradient of the rockfill in the joint, leading to a weak area with a higher tensile strain value in the panel. An optimized range for the single step-type design is recommended to be between 0.375 m and 0.45 m below the junction point. Under static load, the tensile strain and sliding amount of the panel decreased by 12.0 % and 13.37 %, respectively. Under seismic load, the sliding amount of the panel decreased by 16.14 %.

- (3) For the multiple-step design, an optimized range is recommended to be 0.45 m below the junction point. It was found that performance improves when the spacing between the steps is increased. Specifically, with steps of 0.15 m and spacing of 0.15 m, the performance is enhanced. The panel tensile strain and sliding amount decreased by 12.0 % and 14.29 %, respectively, under static load. The sliding amount of the panel decreased by 17.19 % under seismic load.

The adaptability to deformation of panel has been improved through the step-type design, enabling the safety margin of anti-seepage system to be enhanced. The guidance could be offered for the design of anti-seepage joints in pumped storage stations. In the next phase of work, more accurate numerical models will be developed, incorporating the presence of weak layers in the foundation, to obtain more precise design parameters.

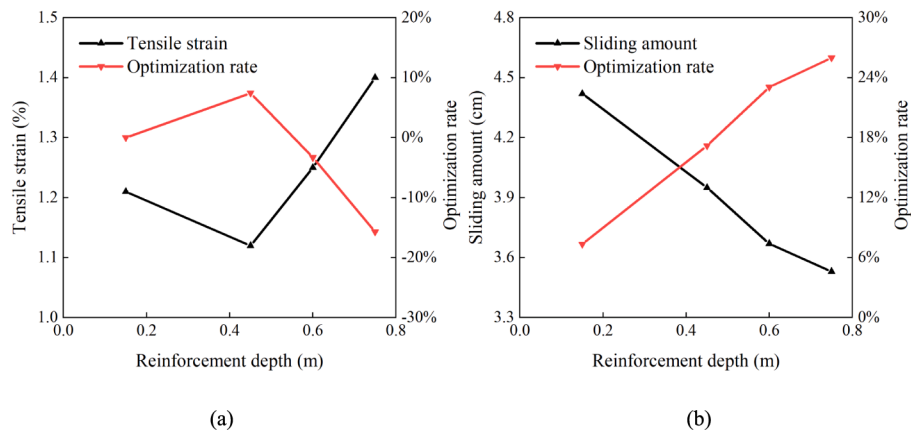


Fig. 28. Deformation of panel joints reinforced by multiple steps ($h = 0.15$ m) under dynamic load: (a) Maximum tensile strain and (b) Dislocation momentum.

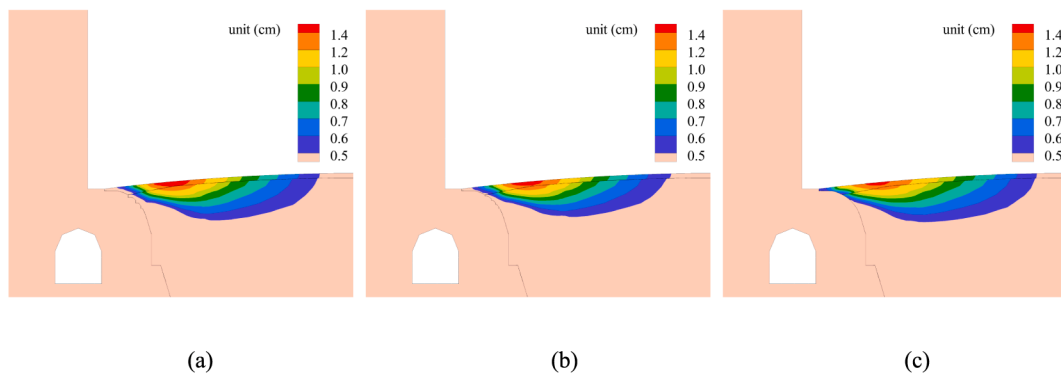


Fig. 29. Horizontal deformation of the joint under dynamic load: (a) $h = 0.15$ m, $H = 0.75$ m, (b) $h = 0.075$ m, $H = 0.75$ m, (c) unreinforced.

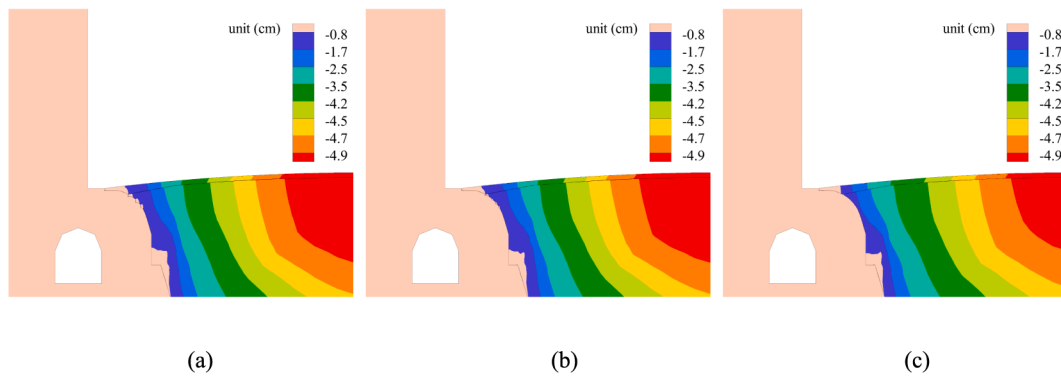


Fig. 30. Vertical settlement of the joint under dynamic load: (a) $h = 0.15$ m, $H = 0.75$ m, (b) $h = 0.075$ m, $H = 0.75$ m, (c) unreinforced.

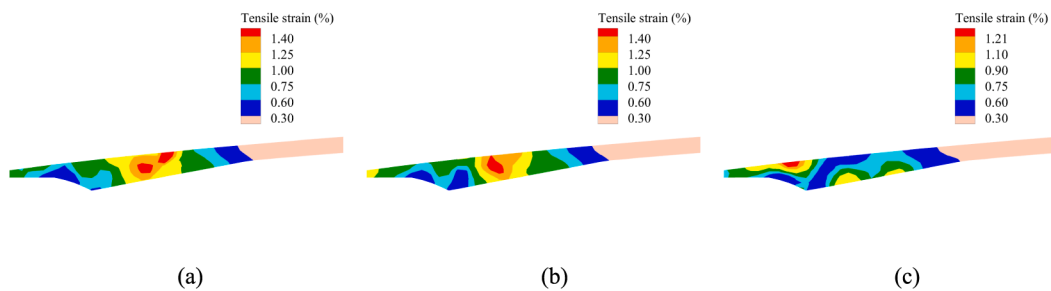


Fig. 31. Panel strain of the joint under dynamic load: (a) $h = 0.15$ m, $H = 0.75$ m, (b) $h = 0.075$ m, $H = 0.75$ m, (c) unreinforced.

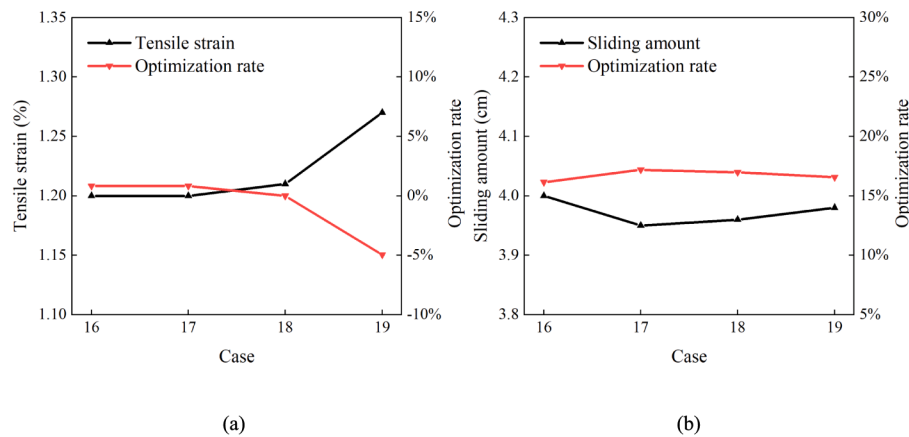


Fig. 32. Deformation of panel joints reinforced by multiple steps under dynamic load: (a) Maximum tensile strain and (b) Dislocation momentum.

CRedit authorship contribution statement

Musen Han: Writing – review & editing, Writing – original draft, Methodology. **Kai Chen:** Writing – review & editing, Funding acquisition. **Yelin Feng:** Project administration. **Degao Zou:** Methodology. **Qingfu Huang:** Investigation.

Declaration of competing interest

The authors declare the following financial interests/personal relationships which may be considered as potential competing interests: [Kai Chen reports writing assistance was provided by Dalian University of Technology. Yelin Feng reports a relationship with Kunming Engineering Corporation Limited that includes: board membership. Degao Zou reports a relationship with Dalian University of Technology that includes: board membership. Qingfu Huang reports a relationship with Kunming Engineering Corporation Limited that includes: board membership. If there are other authors, they declare that they have no known competing financial interests or personal relationships that could have appeared to influence the work reported in this paper].

Data availability

The authors do not have permission to share data.

Acknowledgments

This work was supported by the National Natural Science Foundation of China (Grant Nos. 52350393, 52192674, U2240211) and the Hua Neng Group Science and Technology Project (HNKJ21-HF299).

References

- Billington ED, Basinger DL, Dupuis MJ, Johnson DD, Assoc State Dam Safety Officials; Assoc State Dam Safety O. Real-time location methods for underwater repair of the Ludington Pumped Storage Plant reservoir foundation. 1998 ASDSO Annual Conference - Dam Safety 98. Las Vegas, NV1998. p. 537-48.
- Birk, C., Behnke, R., 2012. A modified scaled boundary finite element method for three-dimensional dynamic soil-structure interaction in layered soil. *Int. J. Numer. Meth. Eng.* 89 (3), 371–402.
- Brecher, C., Fey, M., Tenbrock, C., Daniels, M., 2016. Multipoint constraints for modeling of machine tool dynamics. *Journal of Manufacturing Science and Engineering-Transactions of the Asme.* 138 (5).
- Chen, D., Birk, C., Song, C., Du, C., 2014. A high-order approach for modelling transient wave propagation problems using the scaled boundary finite element method. *Int. J. Numer. Meth. Eng.* 97 (13), 937–959.
- Chen, Z., Li, Z., Wei, Z., 2012. Concurrent multi-scale computational method for damage analyses of civil structures. *Engineering Mechanics.* 29 (10), 205–210.
- Chen, K., Zou, D., Kong, X., Chan, A., Hu, Z., 2017. A novel nonlinear solution for the polygon scaled boundary finite element method and its application to geotechnical structures. *Comput. Geotech.* 82, 201–210.

- Chen, K., Zou, D., Kong, X., Yu, X., 2018. An efficient nonlinear octree SBFEM and its application to complicated geotechnical structures. *Computers and Geotechnics.* 96, 226–245.
- Chen, K., Zou, D., Kong, X., Zhou, Y., 2018. Global concurrent cross-scale nonlinear analysis approach of complex CFRD systems considering dynamic impervious panel-rockfill material-foundation interactions. *Soil Dyn. Earthq. Eng.* 114, 51–68.
- Chen, K., Zou, D., Kong, X., Liu, J., 2019. Elasto-plastic fine-scale damage failure analysis of metro structures based on coupled SBFEM-FEM. *Comput. Geotech.* 108, 280–294.
- Chen, K., Zou, D., Yi, G., Nie, X., Qu, Y., 2024. A flexible mixed-order formula for tetrahedron elements based on SBFEM. *Comput. Geotech.* 171, 106390.
- Degao, Z., Xianjing, K., Bin, X., 2005. User manual for geotechnical dynamic nonlinear analysis. Institute of Earthquake Engineering, Dalian University of Technology, Dalian.
- Development Situation and Outlook of Pumped Storage Power Stations. 2023 International Hydroelectric Development Conference.
- Goswami, S., Becker, W., 2012. Computation of 3-D stress singularities for multiple cracks and crack intersections by the scaled boundary finite element method. *Int. J. Fract.* 175 (1), 13–25.
- Gravenkamp, H., Saputra, A.A., Song, C., Birk, C., 2017. Efficient wave propagation simulation on quadtree meshes using SBFEM with reduced modal basis. *International Journal for Numerical Methods in Engineering.* 110 (12), 1119–1141.
- Guo, N., Zhao, J., 2014. A coupled FEM/DEM approach for hierarchical multiscale modelling of granular media. *Int. J. Numer. Meth. Eng.* 99 (11), 789–818.
- Guo, N., Zhao, J., 2016. Multiscale insights into classical geomechanics problems. *Int. J. Numer. Anal. Meth. Geomech.* 40 (3), 367–390.
- Hao JT, Experimental study on sliding joints of asphalt concrete anti-seepage panels. *Journal of China Institute of Water Resources and Hydropower Research.* (in Chinese).
- International Renewable Energy Agency. Energy transformation 2050. Germany: International Renewable Energy Agency, 2020.
- Javed, M.S., Ma, T., Jurasz, J., Amin, M.Y., 2020. Solar and wind power generation systems with pumped hydro storage: Review and future perspectives. *Renew. Energy* 148, 176–192.
- Lee, K.W., Chong, T.H., Park, G.J., 2003. Development of a methodology for a simplified finite element model and optimum design. *Comput. Struct.* 81 (14), 1449–1460.
- Li, J., Liu, Y., Lin, G., 2023. Implementation of a coupled FEM-SBFEM for soil-structure interaction analysis of large-scale 3D base-isolated nuclear structures. *Comput. Geotech.* 162, 105669.
- Li, Z., Wang, Y., Wu, B., Wang, C., Chen, Z., 2010. Multi-scale modeling and analyses on structural deterioration and damage in long-span bridges and its application. *Acta Mech. Solida Sin.* 31 (6), 731–756.
- Liu, Z., Bessa, M.A., Liu, W.K., 2016. Self-consistent clustering analysis: An efficient multi-scale scheme for inelastic heterogeneous materials. *Comput. Methods Appl. Mech. Eng.* 306, 319–341.
- Liu, J., Lin, G., Li, J., 2012. Short-crested waves interaction with a concentric cylindrical structure with double-layered perforated walls. *Ocean Eng.* 40, 76–90.
- Liu, J., Lin, G., 2012. A scaled boundary finite element method applied to electrostatic problems. *Eng. Anal. Bound. Elem.* 36 (12), 1721–1732.
- Liu, J., Kong, X., Zou, D., 2015. Effects of interface models on deformation of interface between slab and cushion layer and slab stress of concrete faced rock fill dam. *Chinese Journal of Geotechnical Engineering.* 37 (4), 700–710.
- Liu, J., Zhang, P., Lin, G., Wang, W., Lu, S., 2016. High order solutions for the magneto-electro-elastic plate with non-uniform materials. *Int. J. Mech. Sci.* 115, 532–551.
- Liu, J., Zou, D., Kong, X., 2018. Three-dimensional scaled memory model for gravelly soils subject to cyclic loading. *J. Eng. Mech.* 144 (3).
- Lu, S., Liu, J., Lin, G., Wang, W., 2015. Time-domain analyses of the layered soil by the modified scaled boundary finite element method. *Struct. Eng. Mech.* 55 (5), 1055–1086.
- Mao, K.M., Sun, C.T., 1991. A refined global local finite-element analysis method. *Int. J. Numer. Meth. Eng.* 32 (1), 29–43.
- Martin, J.R., Deschapelles, B., 2014. New finite element for steel shear plate analysis. *J. Eng. Mech.* 140 (2), 418–425.

- Natarajan, S., Dharmadhikari, P., Annabattula, R.K., Zhang, J., Ooi, E.T., Song, C., 2020. Extension of the scaled boundary finite element method to treat implicitly defined interfaces without enrichment. *Comput. Struct.* 229, 106159.
- Natarajan, S., Song, C., 2013. Representation of singular fields without asymptotic enrichment in the extended finite element method. *Int. J. Numer. Meth. Eng.* 96 (13), 813–841.
- Ooi, E.T., Shi, M., Song, C., Tin-Loi, F., Yang, Z.J., 2013. Dynamic crack propagation simulation with scaled boundary polygon elements and automatic remeshing technique. *Eng. Fract. Mech.* 106, 1–21.
- Ooi, E.T., Song, C., Tin-Loi, F., 2014. A scaled boundary polygon formulation for elastoplastic analyses. *Comput. Methods Appl. Mech. Eng.* 268, 905–937.
- Ooi, E.T., Natarajan, S., Song, C., Ooi, E.H., 2016. Dynamic fracture simulations using the scaled boundary finite element method on hybrid polygon-quadtree meshes. *Int. J. Impact Eng.* 90, 154–164.
- Pan, G., Gu, W., Zhang, H., Qiu, Y., 2020. Electricity and hydrogen energy system towards accomodation of high proportion of renewable energy. *Automation of Electric Power Systems.* 44 (23), 1–10.
- Qu, Y., Zou, D., Kong, X., Yu, X., Chen, K., 2020. Seismic cracking evolution for anti-seepage face slabs in concrete faced rockfill dams based on cohesive zone model in explicit SBFEM-FEM frame. *Soil Dyn. Earthq. Eng.* 133, 106106.
- Qu, Y., Zou, D., Chen, K., Liu, J., 2021. Three-dimensional refined analysis of seismic cracking and anti-seismic measures performance of concrete face slab in CFRDs. *Computers and Geotechnics.* 139, 104376.
- Saputra, A.A., Birk, C., Song, C., 2015. Computation of three-dimensional fracture parameters at interface cracks and notches by the scaled boundary finite element method. *Eng. Fract. Mech.* 148, 213–242.
- Tu, F., Ling, D., Hu, C., Zhang, R., 2017. DEM-FEM analysis of soil failure process via the separate edge coupling method. *International Journal for Numerical and Analytical Methods in Geomechanics.* 41 (9), 1157–1181.
- Vorobiov, O., Tabatabaei, S.A., Lomov, S.V., 2017. Mesh superposition applied to meso-FE modelling of fibre-reinforced composites: Cross-comparison of implementations. *Int. J. Numer. Meth. Eng.* 111 (11), 1003–1024.
- Wolf, J.P., Song, C.M., 2000. The scaled boundary finite-element method— a primer: derivations. *Comput. Struct.* 78 (1–3), 191–210.
- Wolf, J.P., Song, C.M., 2001. The scaled boundary finite-element method—a fundamental solution-less boundary-element method. *Comput. Methods Appl. Mech. Eng.* 190 (42), 5551–5568.
- Xu, H., Zou, D., Kong, X., Hu, Z., 2016. Study on the effects of hydrodynamic pressure on the dynamic stresses in slabs of high CFRD based on the scaled boundary finite-element method. *Soil Dyn. Earthq. Eng.* 88, 223–236.
- Xu, H., Zou, D., Kong, X., Su, X., 2017. Error study of Westergaard's approximation in seismic analysis of high concrete-faced rockfill dams based on SBFEM. *Soil Dyn. Earthq. Eng.* 94, 88–91.
- Xu, H., Zou, D., Kong, X., Hu, Z., Su, X., 2018. A nonlinear analysis of dynamic interactions of CFRD-compressible reservoir system based on FEM-SBFEM. *Soil Dyn. Earthq. Eng.* 112, 24–34.
- Zhang, P.Z., Sun, B.Y., Gu, Q., Ou, J.P., 2017. Refined aseismic analysis of low-ductility RC frame building based on numerical substructure method. *Engineering Mechanics.* 34, 38–48.
- Zou, D., Xu, B., Kong, X., Liu, H., Zhou, Y., 2013. Numerical simulation of the seismic response of the Zipingpu concrete face rockfill dam during the Wenchuan earthquake based on a generalized plasticity model. *Comput. Geotech.* 49, 111–122.
- Zou, D., Chen, K., Kong, X., Liu, J., 2017. An enhanced octree polyhedral scaled boundary finite element method and its applications in structure analysis. *Eng. Anal. Bound. Elem.* 84, 87–107.
- Zou, D., Teng, X., Chen, K., Yu, X., 2018. An extended polygon scaled boundary finite element method for the nonlinear dynamic analysis of saturated soil. *Eng. Anal. Bound. Elem.* 91, 150–161.
- Zou, D., Chen, K., Kong, X., Yu, X., 2019. An approach integrating BIM, octree and FEM-SBFEM for highly efficient modeling and seismic damage analysis of building structures. *Eng. Anal. Bound. Elem.* 104, 332–346.
- Zou, D., Qu, Y., Kong, X., Chen, K., Liu, J., Gong, J., 2023. Refined analysis on stress state of cutoff wall of high asphaltic core dam on super-deep overburden. *Rock Soil Mech.* 44 (6), 1826–1836.